

Globular clusters in ORBIT: complete dynamical characterisation of the globular cluster population of the Milky Way through updated orbital reconstruction

M. De Leo^{1,2,3,4,*}, M. Zoccali^{3,4}, J. Olivares-Carvajal^{3,4}, B. Acosta-Tripailao^{3,4}, F. Gran⁵, and R. Contreras-Ramos^{3,4}

¹ Dipartimento di Fisica e Astronomia, Università degli Studi di Bologna, Via Piero Gobetti 93/2, Bologna, 40129, Italy

² Osservatorio di Astrofisica e Scienza dello Spazio di Bologna, INAF, Via Piero Gobetti 93/3, Bologna, 40129, Italy

³ Instituto de Astrofísica, Pontificia Universidad Católica de Chile, Av. Vicuña Mackenna 4860, 782-0436, Macul, Santiago, Chile

⁴ Instituto Milenio de Astrofísica MAS, Av. Vicuña Mackenna 4860, 782-0436, Macul, Santiago, Chile

⁵ Université Côte d’Azur, Observatoire de la Côte d’Azur, CNRS, Laboratoire Lagrange, 06304 Nice, France

Received xxx

ABSTRACT

Context. In hierarchical structure formation, the content of a galaxy is determined both by its in-situ processes and by material added via accretions. Globular clusters in particular represent a window for the study of the different merger events that a galaxy underwent. Establishing the correct classification of in-situ and accreted tracers, and distinguishing the various different progenitors that contributed to the accreted population are important tools to deepen our understanding of galactic formation and evolution.

Aims. Our aim is to refine our knowledge of the assembly history of the Milky Way by studying the dynamics of its globular cluster population and establishing an updated classification among in-situ objects and the different merger events identified.

Methods. We used a custom built orbit integrator to derive precise orbital parameters, integrals of motions and adiabatic invariants for the globular cluster sample studied. By properly accounting for the rotating bar, which transforms the underlying model in a time-varying potential, we proceeded to a complete dynamical characterisation of the globular clusters.

Results. We present a new catalogue of clear associations between globular clusters and structures (both in-situ and accreted) in the Milky Way, and a full table of derived parameters. By using all dynamical information available, we were able to attribute previously unassociated or misclassified globular clusters to the different progenitors, including those responsible for the Aleph, Antaeus, Cetus, Elqui, and Typhon merger events.

Conclusions. By using a custom built orbit integrator and properly accounting for the time-varying nature of the Milky Way potential, we have shown the depth of information that can be extracted from a purely dynamical analysis of the globular clusters of our Galaxy. By merging our dynamical analysis with complementary chronochemical studies, we will be able to uncover the remaining secrets of the accretion history of the Milky Way.

Key words. Methods: numerical – Celestial mechanics – Galaxy: kinematics and dynamics – Galaxy: formation – globular clusters: general – Galaxy: structure

1. Introduction

In the prevailing paradigm of Λ Cold Dark Matter (Λ CDM) the structure of the Universe is believed to have formed hierarchically (Peebles 1965; Peebles & Yu 1970), with the largest overdensities accreting smaller neighbours and becoming the present-day massive galaxies (White & Rees 1978; Read et al. 2006). This turbulent process leaves traces that can be studied and decoded in the stellar and globular cluster (GC) populations of the final surviving galaxy and these traces allow to identify the properties and contribution of the populations formed “in-situ” and of the accreted material from the mergers (Eggen et al. 1962; Searle & Zinn 1978; Bullock & Johnston 2005). Our Galaxy, the Milky Way (MW), provides a privileged window through which we can peer at the processes shaping galactic evolution and formation by studying the stellar and GC populations present. Due to the complexities of stellar and cluster formation, GCs offer a better opportunity of studying the merger history and accreted content of a galaxy (e.g. Belokurov & Kravtsov 2024,

and references therein). To this end, it is of paramount importance to discriminate between in-situ and accreted GCs. First studies aimed at distinguishing the two families used available chemical and spatial information (Zinn 1985, 1996), later the availability of more accurate chemical data and age estimations opened up the way for the use of Age-Metallicity Relations (AMR, Marín-Franch et al. 2009; Forbes & Bridges 2010; Leaman et al. 2013). Running in parallel to the chronochemical techniques, the availability of samples with complete position and velocity information allowed the use of Integrals of Motions (IoM) and adiabatic invariants (such as the actions), conserved after the mergers, to isolate substructures in dynamical parameter spaces (Helmi & White 1999; Helmi & de Zeeuw 2000; Binney & Tremaine 2008; Gómez et al. 2010). Concurrently, the “accreted” family was further split up with more detailed identifications of the first confirmed mergers, Sagittarius (Ibata et al. 1994) and the so-called “Helmi Streams” (Helmi et al. 1999). The floodgates of discovery were opened with the data releases of the *Gaia* mission (Gaia Collaboration et al. 2016), providing position and velocity information for millions of targets, and with complementary wide spectroscopic surveys (chief among

* micheledl89@gmail.com

them the Apache Point Observatory Galactic Evolution Experiment, APOGEE, Majewski et al. 2017). These led to the identification of several different candidate merger events, a research that is still ongoing due to the continuous discovery of new structures. The seminal work of Massari et al. (2019) set off systematic efforts to classify the merger events, characterise them in the different parameter spaces, and establish affiliations between the MW GCs and the different progenitors. Refined research techniques using clustering algorithms (Lövdal et al. 2022; Ruiz-Lara et al. 2022; Dodd et al. 2023) enabled the identification of many new substructures. Robust spectroscopic and photometric analysis allow ever more precise estimations of the age and chemical composition of stars and GCs (Horta et al. 2023; Massari et al. 2023; Ceccarelli et al. 2024) facilitating the establishment of links with the different progenitors. One often overlooked piece of the puzzle is the potential model used to derive the orbital parameters, the IoMs and the adiabatic invariants. To properly capture the inherent intricacies of the structure of the MW it is necessary to incorporate all observed components of the Galaxy. In particular, the rotating bar is a crucial player both for the direct effect it has on the inner regions of the MW and for the time-varying nature of its action that creates resonances (Chiba et al. 2021; Chiba & Schönrich 2021; Trick 2022; Dillamore et al. 2024). We have developed the ORBITAL INTEGRATION TOOL (ORBIT) as a flexible, transparent and efficient code to perform orbit integrations with static and time-varying MW potentials. ORBIT has been employed in Olivares Carvajal et al. (2024) to study the RR Lyrae bulge population and this paper presents our first results on the MW GCs. This work is but a stepping stone towards a deeper understanding of how perturbations and time-varying components of the MW potentials shape and affect the inventory and structure of our Galaxy.

In Section 2 we present the data catalogues used, Section 3 contains an in-depth description of ORBIT and the underlying potential model it uses, Section 4 contains our results, which we discuss in Section 5 while Section 6 has a summary of our conclusions.

2. Data

The main source of the data used throughout this work is the extensive repository of GC parameters by Baumgardt et al.¹ (Baumgardt 2017; Baumgardt & Hilker 2018; Baumgardt & Vasiliev 2021; Vasiliev & Baumgardt 2021). For all the GCs in the Gran “family” we use the MUSE (Stuik et al. 2006; Bacon et al. 2010; Ströbele et al. 2012; Hartke et al. 2020) radial velocities reported by Gran et al. (2024) in place of those reported in the Baumgardt repository. We do the same with VVV-CL001, using the radial velocity from MUSE data reported in Olivares Carvajal et al. (2022). Likewise, for Patchick 126 and VVV-CL160, we use the proper motions and radial velocities measured with a combination of Gaia DR3 (Gaia Collaboration et al. 2023), VVV-X (Minniti et al. 2010; Saito et al. 2012) and IGRINS (Park et al. 2014; Mace et al. 2018) by Garro et al. (2023). Finally, we complement the sample with a few additions from more recent works: VVV-CL002 (Moni Bidin et al. 2011; Minniti et al. 2021, 2024), Gran 4 (Gran et al. 2022, 2024), ESO 93-08 (Garro et al. 2023), and Patchick 122 (Garro et al. 2022, 2023).

We transform the observed positions, distances and 3D velocities to the Galactocentric reference frame assuming the velocity vector of the Sun to be $(U_{\odot}, V_{\odot}, W_{\odot}) =$

$(11.1, 12.24, 7.25) \text{ km s}^{-1}$ (Schönrich et al. 2010), the velocity of the Local Standard of Rest $V_{LSR} = 220 \text{ km s}^{-1}$ (Reid 2008), the distance of the Sun from the Galactic Center $R_{\odot} = 8.20 \text{ kpc}$ (GRAVITY Collaboration et al. 2019), and the height of the Sun above the Galactic Plane $z_{\odot} = 20.8 \text{ pc}$ (Bennett & Bovy 2019).

The vast majority (90%) of the sample has observational errors on distances, radial velocities and proper motions along the α and δ directions of, respectively, less than 1 kpc, 2 km/s, 0.1 mas/yr, and 0.05 mas/yr. We tested that the observational errors have a negligible impact on the classification of the GCs inside the various progenitor families and show in Appendix A that this is true even for the GCs with the highest uncertainties on distance (AM 1, Eridanus, Palomar 3 and Palomar 4) and kinematical values (2MASS-GC01, AM 1 and Patchick 122).

3. Method

The study of the GC population in this paper is conducted mainly using the custom-made code ORBIT. As the name implies, ORBIT is a code for orbit integrations and was designed to be customizable based on the needs of the problem to be tackled. The decision to develop and use a custom code in place of using a well established one like GALPY (Bovy 2015) or AGAMA (Vasiliev 2019a) stems from the desire to have complete control over the Galactic model used, on every step of the orbit integration and on the available outputs. This allows us to gauge sources of errors as transparently and completely as possible and properly evaluate realistic uncertainties on the parameters derived through the integration.

The orbital history of the GCs is computed with ORBIT backwards in time for 10 Gyr (to allow all GCs to complete more than one orbit) with a timestep of 10^4 yrs. The recovered orbital parameters (see subsection 3.3) are then used to identify the most likely progenitors for each GC. Starting from the classification of Massari et al. (2019), we reassess the various orbital families and established memberships, focusing on relatively new GCs and on previously known ones with uncertain ancestry.

3.1. General information on ORBIT

ORBIT is a code written in the C computing language and it uses a “leap-frog” integration, specifically of the “kick-drift-kick” type. This choice is driven by the fact that this is a type of modified Verlet integration (Verlet 1967; Binney & Tremaine 2008) that fulfills two very important prerequisites for dynamical modeling: it is inherently time-reversible, thus allowing for both backward and forward integrations, and it suppresses numerical errors at each step (Roberts & Quispel 1992; Hairer et al. 2003). Taken together, these characteristics ensure that the IoMs do not drift over time due to errors in the numerical approximation at each step and thus the evolution stays accurate over extremely long integrations made of a large number of steps.

The “leap-frog kick-drift-kick” scheme first computes the velocities of the tracers at the half-step $n + 1/2$, then the positions and accelerations at the full step $n + 1$ and then updates the velocities at the full step. This scheme ensures a good approximation of the evolution of the system while only doing one time per step the computationally expensive acceleration calculations. We note here that, while this is optimal for our use case and current model, it might not be the best solution when taking into account effects that explicitly depend on the velocity of tracers, such as dynamical friction for satellite galaxies

¹ <https://people.smp.uq.edu.au/HolgerBaumgardt/globular/>

(Chandrasekhar 1943a,b,c). This is because adding dynamical friction (which depends on velocity, so the needed calculations would be performed twice for each timestep) would slow down the integration time. From a dynamical perspective, it has been demonstrated that dynamical friction has a negligible effect on the orbits of most GCs (Moreno et al. 2022) with very few exceptions for the lowest energy ones (which would be classified as bulge GCs anyway).

ORBIT requires as initial conditions the 6D Galactocentric phase space coordinates of the tracers (X, Y, Z, V_x, V_y, V_z)_{gal}. The number of timesteps and number of tracers can be specified in a parameter file without recompiling the source code, the step size can be modified inside the source code and requires recompiling. The source code is designed to compile without errors or warnings on the most common versions of the GNU Compiler Collection (GCC)² and has been tested and verified on Windows and Linux operating systems. The classic sanity check of the conservation of IoMs during integration is reported in Appendix B

3.2. Galactic potential model

The model of the MW gravitational potential employed in ORBIT is composed of a Navarro-Frenk-White (NFW) Dark Matter (DM) halo (Navarro et al. 1996), two Miyamoto-Nagai (MN) stellar discs (Miyamoto & Nagai 1975), two MN gaseous discs, a Long-Murali (LM) rotating bar (Long & Murali 1992) and a spherical bulge component modeled as an Plummer profile (Plummer 1911). Finally, but with a negligible impact on the final results, the central black hole of our galaxy is present as a point source with mass $M_{BH} = 4.154 \times 10^6 M_\odot$ (GRAVITY Collaboration et al. 2019).

The NFW DM halo is the most massive component of the potential with mass $M_{DM} = 8.0 \times 10^{11} M_\odot$, scale radius $r_s = 16$ kpc and halo concentration parameter $c = 15.3$. All the parameter values chosen are quite commonly used, i.e. in the MWPotential2014 from Bovy (2015).

The two MN stellar discs are set up to reproduce the observed thin and thick disc of the MW, their scale heights are fixed at $z_{thin} = 0.3$ kpc and $z_{thick} = 0.9$ kpc (i.e. McMillan 2017) and their masses and scale lengths are chosen to recover the local mass densities measured by Lian et al. (2022): $M_{thin} = 3.65 \times 10^{10} M_\odot$, $M_{thick} = 1.55 \times 10^{10} M_\odot$, $a_{thin} = 3.5$ kpc and $a_{thick} = 2.0$ kpc.

The two MN gaseous discs represent the HI and molecular gas discs observed in the MW with their masses (for a total gas mass of $M_{gas} = 1.22 \times 10^{10} M_\odot$) and scale heights fixed to the same values as the gas discs in McMillan (2017), $z_{HI} = 0.085$ kpc and $z_{HII} = 0.045$ kpc. Like their stellar counterparts, their scale lengths are set to reproduce the local mass densities measured for the respective gases (i.e. McKee et al. 2015), $a_{HI} = 1.824$ kpc and $a_{HII} = 5.895$ kpc.

The bulge of our model is composed of both a bar and a spherical component. The LM bar has a mass of $M_{bar} = 1.0 \times 10^{10} M_\odot$, is geometrically similar to the single-bar model in Wegg et al. (2015), with semiaxes $a_{bar} = 5.5$, $b_{bar} = 0.68$, $c_{bar} = 0.09$ kpc, an inclination angle $\alpha_{bar} = 30^\circ$ and rotating with a pattern speed $\Omega_p = 41.3 \pm 3 \text{ km s}^{-1} \text{ kpc}^{-1}$ (Sanders et al. 2019). Recent studies (i.e. Haywood et al. 2024) put the bar formation at 8-10 Gyr ago, we tested that the results of this work don't change between running the integration for 8 Gyr or for 10 Gyr. The exceptions are a few high apoc-

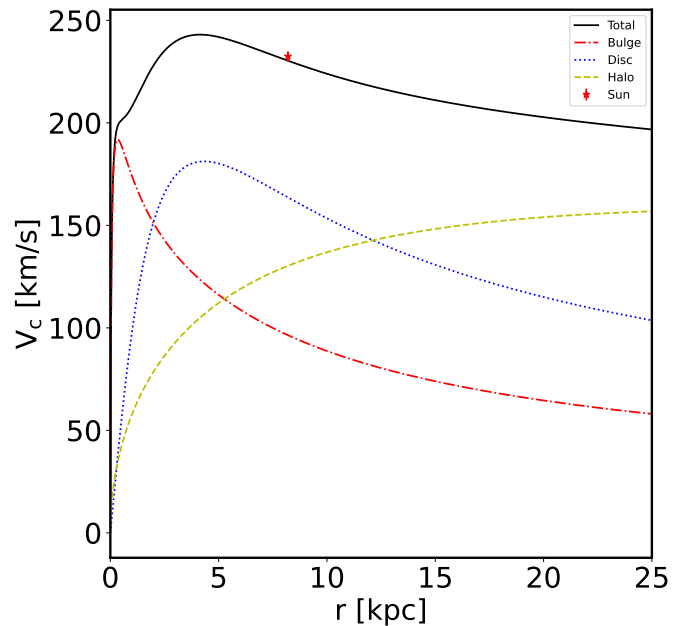


Fig. 1: Rotational curve of the MW. In solid black the velocity of the full potential model, the yellow dashed line is the contribution from the halo component, the blue dotted line is the total contribution from the discs and the red dash-dotted is the contribution from the bulge (bar and spheroid), the red symbol with errorbar represents the Sun.

entre GCs (AM 1, Crater, Palomar 3, Palomar 4 and Sagittarius II) that complete only a few orbits in the total integration time, thus the orbital parameters are slightly more accurate with the longer integration. The evolution of the bar during its lifetime, including the change in pattern speed (Chiba et al. 2021) will be the topic of future work. The spherical component has a mass of $M_{sph} = 1.0 \times 10^{10} M_\odot$ and a scale radius of $a_{sph} = 0.3$ kpc. The geometrical parameters of both the bar and the spherical component are fitted to the Wegg et al. (2015) single-bar model which reproduced the observed density distribution of red clump giants in a boxy/peanut bulge shape.

The choice to include a spherical component to the bulge is motivated by the observations of the MW bulge stellar populations (Valenti et al. 2016; Zoccali et al. 2018; Lim et al. 2021; Queiroz et al. 2021; Zoccali et al. 2024; Prudil et al. 2025). The total mass of the MW bulge chosen reflects the considerations made in Shen & Zheng (2020) and the equal split between the bar and spherical component follows Zoccali et al. (2018). Fig. 1 shows the rotation curve of the Galaxy produced by our model (including the individual contributions of the different components) which is consistent with the rotation of the Sun (red star with errorbar, from Schönrich et al. 2010).

3.3. Outputs

ORBIT can be customised to have a wide variety of outputs. In its most common form it provides all the classical orbital parameters, the actions and the circularity of each tracer and it can also output a full orbital history recording the 6D spatial information of each tracer at every timestep.

Given that the underlying potential is non-static, we expect the apocentre, R_{apo} , and pericentre, R_{peri} , (and therefore the ec-

² <https://gcc.gnu.org/>

centricity, ecc) of the tracers to vary in time, making the significance of the recovery of a single value for these parameters quite uncertain in its physical meaning. To work around this fact, the code computes R_{apo} , R_{peri} , ecc for each complete orbit of each tracer, thus producing a distribution of values. The mean and the standard deviation of each distribution are then, respectively, the final output and the uncertainty for each parameter. Quasi-periodic and more “well-behaved” tracers will have experienced a smaller variation in the parameter values and have small uncertainties while tracers on chaotic orbits will have larger errors.

The actions (J_R, J_θ, J_ϕ) are computed following Binney & Tremaine (2008):

$$J_\phi = L_z, \quad (1)$$

$$J_\theta = L - |L_z|, \quad (2)$$

$$J_R = \frac{2}{\pi} \int_{R_{peri}}^{R_{apo}} \sqrt{2E - 2\Phi(r) - \frac{L^2}{r^2}} dr, \quad (3)$$

where L is the total angular momentum and the integral for J_R is solved numerically with a composite Simpson’s 1/3 rule (Atkinson 1991).

We exploit the calculation of the actions to compute:

$$J_{tot} = J_R + J_\theta + |J_\phi|, \quad (4)$$

$$J_\perp = \frac{J_\theta - J_R}{J_{tot}}, \quad (5)$$

$$J_\parallel = \frac{J_\phi}{J_{tot}}, \quad (6)$$

these ancillary parameters allow us to explore the “projected action space map” where J_\parallel is the normalised z -component of the angular momentum and J_\perp gauges the relative importance of radial and vertical motions (Vasiliev 2019b; Naidu et al. 2020; Malhan et al. 2022).

The circularity ε is defined as the ratio of the tracer angular momentum over the angular momentum of a maximally rotating planar orbit having the same specific energy as the tracer (Abadi et al. 2003; Ruchti et al. 2014; Orkney et al. 2023):

$$\varepsilon = \frac{L_z}{L_z^{max}(E)}, \quad (7)$$

where $L_z^{max}(E)$ is found by identifying the (V_c, R_c) pair that minimises the following equation for the energy of the tracer:

$$\left| \frac{V_c^2}{2} + \Phi(R_c, 0) - E \right|, \quad (8)$$

with V_c being the circular velocity defined as:

$$V_c = \sqrt{R_c \cdot \frac{\delta\Phi}{\delta R} \Big|_{R_c}}, \quad (9)$$

The full list of parameters computed with ORBIT and used throughout this work is as follows: R_{peri} , R_{apo} , ecc , $|Z_{max}|$ (the maximum excursion from the Galactic plane), E_{tot} , L_x , L_y , L_z , L , L_\perp (the axial, total, and perpendicular angular momenta), J_ϕ , J_θ , J_R , J_{tot} , J_\perp , J_\parallel , ε . Due to the choice of the orientation of the Galactocentric reference frame axes employed in this work, prograde tracers have negative L_z , J_ϕ and ε while retrograde tracers have positive values of these parameters.

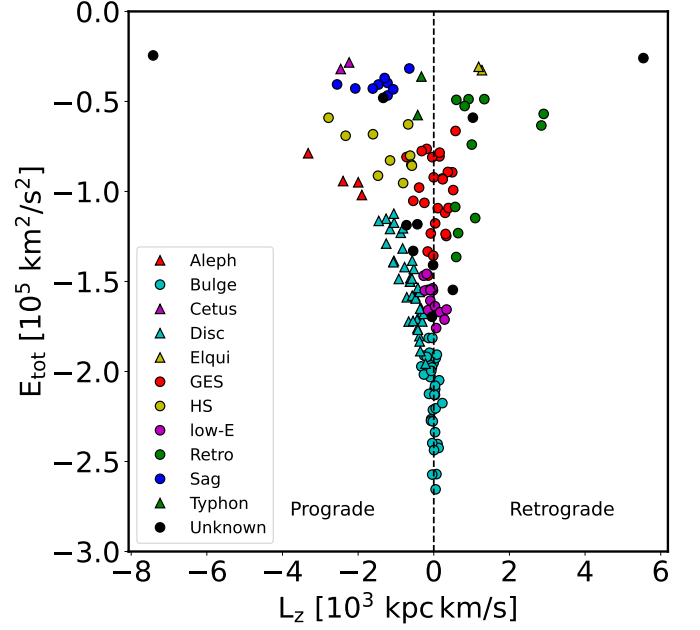


Fig. 2: The GC sample in the angular momentum versus total energy plane. As per the legend, the GCs are marked based on their affiliation to a progenitor: red triangles for Aleph, cyan circles for the bulge, purple triangles for Cetus, cyan triangles for the disc, yellow triangles for Elqui, red circles for Gaia-Enceladus-Sausage (GES), yellow circles for the Helmi Streams (HS), purple circles for the low energy group (low-E), green circles for the retrogrades (retro), blue circles for Sagittarius (Sag), green triangles for Typhon, black circles for the unassociated. The dashed line at $L_z = 0$ guides the eye in dividing the prograde and retrograde sides.

4. Results

Recent studies on the non-conservation of the IoMs in the MW (i.e. Pagnini et al. 2023; Woudenberg & Helmi 2025; Dillamore & Sanders 2025) due to the mergers, secular evolution of the Galaxy, effect of the rotating bar and a few other factors put into question the accuracy of dynamical analysis. This is the principal reason why, instead of focusing on only the IoMs and/or adiabatic invariants, this work presents a full sample of dynamical spaces (6 spaces for 10 different parameters) that helps in characterising the various progenitors. For each one of the progenitors, due to differences in the way the accretion event happened, its age, the mass of the accreted structure, and many other factors, there will be different signatures in different parameter spaces. The ability to explore a vast, multidimensional parameter space is fundamental in highlighting features and trends that allow to discriminate between the numerous orbital families present in our Galaxy.

The main results of our orbital analysis are summarised in Table 1, where we list the GCs studied and their most likely progenitor. Figure 2 gives a quick overview of the composition of the orbital families in the commonly used $L_z - E_{tot}$ space. Throughout this section we will point out the main signatures in the various parameter spaces of the most important substructures inside the MW and provide boundaries for the values of the dynamical parameters deemed most important in assigning the GC to a given progenitor. To decide if a GC belongs to one family or

Table 1: Identification of globular cluster progenitors based on the dynamical analysis carried on in this paper.

Cluster	Progenitor	Cluster	Progenitor	Cluster	Progenitor	Cluster	Progenitor
2MASS-GC01	Disc	NGC 4590	HS	NGC 6362	Disc	NGC 6864	GES
2MASS-GC02	Disc	NGC 4833	GES	NGC 6366	Disc	NGC 6934	Unk
AM 1	Elqui	NGC 5024	HS	NGC 6380	Bulge	NGC 6981	GES
AM 4	Unk	NGC 5053	HS	NGC 6388	low-E	NGC 7006	Retro
Arp 2	Sag	NGC 5139	Retro/Thamnos	NGC 6397	Disc	NGC 7078	Disc
BH 140	Unk	NGC 5272	HS	NGC 6401	Bulge	NGC 7089	GES
BH 261	Disc	NGC 5286	GES	NGC 6402	low-E	NGC 7099	GES
Crater	Unk	NGC 5466	Retro	NGC 6426	HS	NGC 7492	GES
Djor 1	Unk	NGC 5634	HS	NGC 6440	Bulge	Pal 1	Aleph
Djor 2	Bulge	NGC 5694	Retro	NGC 6441	Disc	Pal 2	GES
E 3	Aleph	NGC 5824	HS	NGC 6453	Bulge	Pal 3	Cetus
Eridanus	Sag	NGC 5897	Unk	NGC 6496	Disc	Pal 4	Cetus
ESO 93-08	Aleph/Disc	NGC 5904	GES	NGC 6517	Bulge	Pal 5	HS
ESO 280-SC06	GES	NGC 5927	Disc	NGC 6522	Bulge	Pal 6	Bulge
ESO 452-C11	Bulge	NGC 5946	low-E	NGC 6528	Bulge	Pal 8	Disc
FSR 1713	Disc	NGC 5986	low-E	NGC 6535	low-E	Pal 10	Aleph/Disc
FSR 1735	Disc	NGC 6093	low-E	NGC 6539	Disc	Pal 11	Disc
FSR 1758	Retro/Thamnos	NGC 6101	Retro/Antaeus	NGC 6540	Bulge	Pal 12	Sag
Gran 1	Bulge	NGC 6121	GES	NGC 6541	Disc	Pal 13	Retro
Gran 2	Retro/Thamnos	NGC 6139	Disc	NGC 6544	low-E	Pal 14	Typhon
Gran 3	Unk	NGC 6155	low-E	NGC 6553	Disc	Pal 15	Typhon
Gran 4	HS	NGC 6171	Disc	NGC 6558	Bulge	Patchick 122	Disc
Gran 5	Bulge	NGC 6205	GES	NGC 6569	Disc	Patchick 126	Disc
HP 1	Bulge	NGC 6218	Disc	NGC 6584	GES/HS	Pyxis	Elqui
IC 1257	GES	NGC 6229	GES	NGC 6624	Bulge	Rup 106	HS
IC 1276	Disc	NGC 6235	Disc	NGC 6626	Bulge	Sag II	Unk
IC 4499	Retro	NGC 6254	Disc	NGC 6637	Bulge	Ter 1	Bulge
Laevens 3	Sag	NGC 6256	Bulge	NGC 6638	Bulge	Ter 2	Bulge
Liller 1	Bulge	NGC 6266	Bulge	NGC 6642	Bulge	Ter 3	Disc
Lynga 7	Disc	NGC 6273	low-E	NGC 6652	Bulge	Ter 4	Bulge
NGC 104	Disc	NGC 6284	Unk	NGC 6656	Disc	Ter 6	Bulge
NGC 288	Retro	NGC 6287	low-E	NGC 6681	low-E	Ter 7	Sag
NGC 362	GES	NGC 6293	Bulge	NGC 6712	low-E	Ter 8	Sag
NGC 1261	GES	NGC 6304	Disc	NGC 6715	Sag	Ter 9	Bulge
NGC 1851	GES	NGC 6316	Disc	NGC 6717	Bulge	Ter 10	low-E
NGC 1904	GES	NGC 6325	Bulge	NGC 6723	Unk	Ter 12	Disc
NGC 2298	GES	NGC 6333	low-E	NGC 6749	Disc	Ton 2	Disc
NGC 2419	Sag	NGC 6341	GES	NGC 6752	Disc	UKS-1	GES
NGC 2808	GES	NGC 6342	Bulge	NGC 6760	Disc	VVV-CL001	Bulge
NGC 3201	Retro/Antaeus	NGC 6352	Disc	NGC 6779	GES	VVV-CL002	Bulge
NGC 4147	GES	NGC 6355	Bulge	NGC 6809	low-E	VVV-CL160	GES
NGC 4372	Disc	NGC 6356	Disc	NGC 6838	Disc	Whiting 1	Sag

Notes. The progenitors are the following: Aleph, Antaeus, bulge, Cetus, disc, Elqui, Gaia-Enceladus-Sausage (GES), Helmi Streams (HS), low energy group (low-E), Sagittarius (Sag), retrograde family (retro), Thamnos, Typhon, and unknown (Unk).

another we check which “locus” it tracks across the most dynamical parameter spaces (ideally across all). Here and in the rest of the paper we refer to the locus of a substructure as the region of dynamical space populated by bona fide traces belonging to it. Some parameter spaces don’t explicitly allow to distinguish between prograde and retrograde tracers, but that distinction is often useful to solve apparent overlapping between families (i.e. in Fig. 3 the green circles of retrograde GCs and the yellow circles of Helmi Streams GCs overlap but the two families are clearly discriminated by their sign of L_z). In Sec. 5 we will cover the edge cases of GCs with the most uncertain associations.

4.1. Structures considered and absent progenitors

This work is focused on the following structures: disc and bulge of the MW (making up the in-situ component), Gaia-Enceladus-Sausage (GES, Koppelman et al. 2018; Belokurov et al. 2018; Haywood et al. 2018; Helmi et al. 2018), Sagittarius (Sag, Ibata et al. 1994; Majewski et al. 2003), the Helmi Streams (HS, Helmi et al. 1999; Koppelman et al. 2019b), the retrograde halo (with a detailed discussion in Sec. 5.2), the low energy group (low-E, first labeled by Massari et al. 2019, with a detailed discussion in Sec. 5.1), Aleph (Naidu et al. 2020), Cetus (Newberg et al. 2009; Yuan et al. 2019, 2022), Typhon (Tenachi et al. 2022), and Elqui (Shipp et al. 2018, 2019).

In our analysis we have seemingly ignored some known substructures, either because the progenitor locus substantially

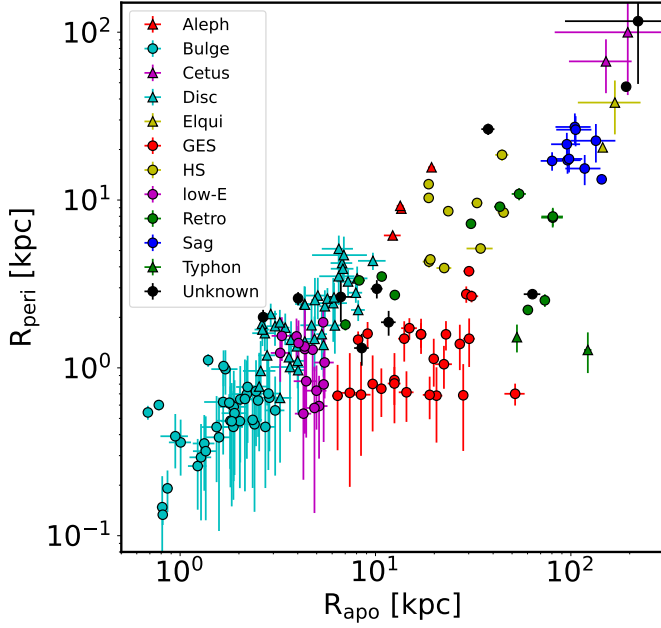


Fig. 3: The GC sample in the apocentre versus pericentre plane, in logarithmic scale. The uncertainties are computed as detailed in Sec. 3.3. The GCs are marked depending on their identified progenitor as in Fig. 2.

overlaps with well known structures or because it was not possible (due to lack or scarcity of data) to properly identify the progenitor locus. In both instances, this made it impossible to dynamically distinguish the newer candidates from the well established structures. For LMS-1/Wukong (Naidu et al. 2020; Yuan et al. 2020), the stellar component identified by Malhan et al. (2024) overlaps with the loci of the HS and GES progenitors in all parameter spaces. The loci identified for Shakti and Shiva (Malhan & Rix 2024) substantially overlap with the disc and low-E groups, while it has not been possible to produce a suitable dataset to identify the loci of Icarus (Re Fiorentin et al. 2021, 2024) and Pontus (Malhan et al. 2022; Malhan 2022). In the case of Nyx (Necib et al. 2020b,a, 2022), we don't include it in our analysis because of the mounting evidence that it is not an independent merger event (Horta et al. 2023; Wang et al. 2023).

4.2. Bulge

The MW Bulge GC population is characterised by having the least energetic GCs (cyan circles in Fig. 2). While all types of orbits (prograde, retrograde or radial) are possible, the value of $|L_z|$ stays close to zero for all members of this group as they reside in the deepest part of the MW potential well. Likewise, having orbits largely confined to the bulge, these GCs occupy the bottom left corner of $R_{apo} - R_{peri}$ space (Fig. 3). We consider as bulge GCs those with:

- $E_{tot} < -1.75 \times 10^5 \text{ km}^2/\text{s}^2$
- $R_{peri} < 1.5 \text{ kpc}$
- $R_{apo} < 3.5 \text{ kpc}$

4.3. Disc

While there are subtle kinematical differences between the populations of tracers inhabiting the thin and the thick discs of the

MW, their dynamical distributions largely overlap and the two structures are better separated through chemical analysis (i.e. Bensby et al. 2014; Hayden et al. 2015). For this reason, in the scope of our present work, we refer to both thin and thick disc populations as belonging to one single structure. The MW disc is quite prominently visible in the prograde portion of $L_z - E_{tot}$ space (cyan triangles in Fig. 2). Consequently, the main features of disc GCs are the $\varepsilon \approx J_{||} \leq -0.5$ (usually two very similar values, as they both gauge the rotational support of an orbit) and $ecc \leq 0.6$. Disc GCs are also well identified in the most prograde sector of $J_{||} - J_{\perp}$ space (Fig. 4) and trace a characteristic sequence in the $R_{peri} - ecc$ space (Fig. 5). Disc GCs generally have the following defining characteristics:

- $-2.0 \times 10^5 \text{ km}^2/\text{s}^2 < E_{tot} < -1.1 \times 10^5 \text{ km}^2/\text{s}^2$
- $L_z > 0 \text{ kpc km/s}$
- $0.6 \text{ kpc} < R_{peri} < 6 \text{ kpc}$
- $Ecc < 0.7$
- $J_{||}/\varepsilon < -0.4$

4.4. Gaia-Enceladus-Sausage (GES)

As the most massive accretion event of our Galaxy, the GES is prominently visible as a central, mildly energetic overdensity in $L_z - E_{tot}$ space (red circles in Fig. 2). The population of GCs associated with this event is characterised by radial orbits (Fig. 4) with high ecc at relatively low R_{peri} (Fig. 5). GES GCs are characterised by:

- $-1.5 \times 10^5 \text{ km}^2/\text{s}^2 < E_{tot} < -0.6 \times 10^5 \text{ km}^2/\text{s}^2$
- $Ecc > 0.7$
- $4 \text{ kpc} < Z_{max} < 40 \text{ kpc}$
- $-0.3 < J_{||}/\varepsilon < 0.3$
- $J_{\perp} < 0.0$

4.5. Sagittarius (Sag)

The ongoing merger of the Sagittarius dwarf galaxy is the most recent accretion event to affect our Galaxy, and it is still ongoing and visible in the sky in the form of a wide, long stellar stream. The GCs associated with the Sag event exhibit highly energetic, prograde orbits (blue circles in Fig. 2), are among those with the highest R_{peri} and R_{apo} (Fig. 3) and also have high L_{\perp} (Fig. 6). We define as Sag GCs those with:

- $E_{tot} > -0.5 \times 10^5 \text{ km}^2/\text{s}^2$
- $-3.0 \times 10^3 \text{ kpc km/s} < L_z < -0.5 \times 10^3 \text{ kpc km/s}$
- $4.0 \times 10^3 \text{ kpc km/s} < L_{\perp} < 7 \times 10^3 \text{ kpc km/s}$

4.6. Helmi Streams (HS)

The progenitor of the Helmi Streams has been one of the first accreted substructures identified through the study of IoMs. The population belonging to this accretion event is characterised by prograde, high-energy orbits between the disc and the Sag populations in $L_z - E_{tot}$ space (yellow circles in Fig. 2). The HS GCs also occupy a well isolated portion of the $L_z - L_{\perp}$ plane (Fig. 6) and a distinctive sequence in $R_{peri} - ecc$ space (Fig. 5). Our selection for the HS GCs is:

- $-1.0 \times 10^5 \text{ km}^2/\text{s}^2 < E_{tot} < -0.5 \times 10^5 \text{ km}^2/\text{s}^2$
- $L_z < -0.5 \times 10^3 \text{ kpc km/s}$
- $1.0 \times 10^3 \text{ kpc km/s} < L_{\perp} < 4.0 \times 10^3 \text{ kpc km/s}$

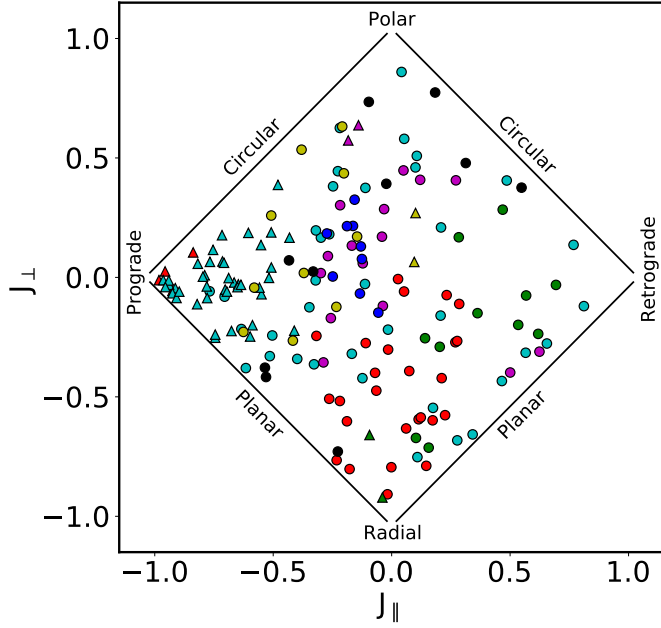


Fig. 4: The GC sample in the parallel versus perpendicular action space. GCs with $J_{||} \approx -1$ are on nearly circular prograde orbits, conversely $J_{||} \approx 1$ identifies nearly circular retrograde orbits. GCs on radial orbits have $J_{\perp} \approx -1$ while those on polar orbits have $J_{\perp} \approx 1$. The GCs are marked depending on their identified progenitor as in Fig. 2.

4.7. Retrogrades

The full characterisation of the retrograde portion of the halo is an ongoing effort that has seen several candidate merger events proposed over recent years. Since some of the candidate progenitors have been discarded, the consensus around others is still ongoing and new ones are being proposed, we refer to Sec. 5.2 for a more in-depth discussion of each progenitor and here we limit ourselves to sketching defining traits of the whole retrograde family. The retrograde GCs can be distinguished clearly in $L_z - L_{\perp}$ space (Fig. 6) and populate a distinctive diagonal streak of increasing ε for decreasing $|Z_{max}|$ (Fig. 7). We identify as members of this group the GCs having:

- $E_{tot} > -1.5 \times 10^5 \text{ km}^2/\text{s}^2$
- $L_z > 0.5 \times 10^3 \text{ kpc km/s}$
- $Z_{max} > 4 \text{ kpc}$

4.8. Low-energy group (low-E)

This group has been associated to various different accretion events and in-situ structures and for the moment we will keep this general label. The GCs associated with this group are characterised by energies lower than the GES but higher than the bulge and small values of $|L_z|$ (purple circles in Fig. 2). Similarly, the GCs in the low-E group populate a region of mid ε and Z_{max} (Fig. 7). Low-E GCs generally have:

- $-1.8 \times 10^5 \text{ km}^2/\text{s}^2 < E_{tot} < -1.4 \times 10^5 \text{ km}^2/\text{s}^2$
- $0.5 \text{ kpc} < R_{peri} < 2 \text{ kpc}$
- $3 \text{ kpc} < R_{apo} < 6 \text{ kpc}$
- $3 \text{ kpc} < Z_{max} < 6 \text{ kpc}$
- $-0.5 < \varepsilon < 0.5$

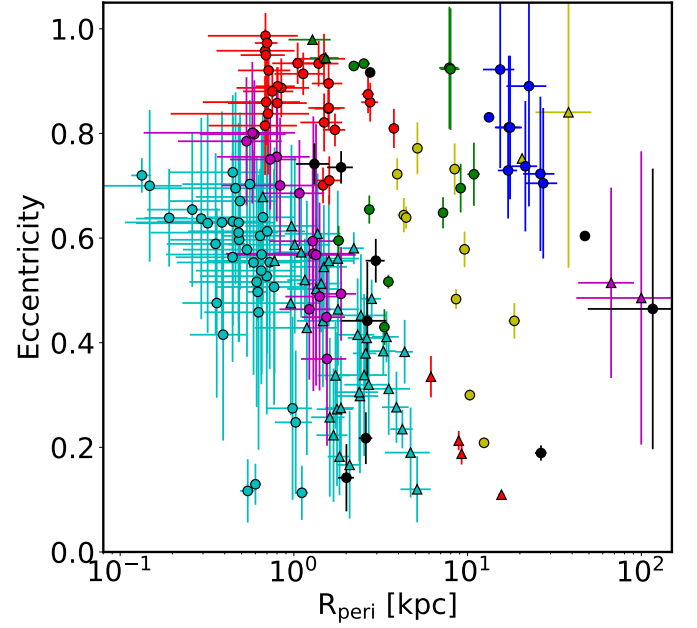


Fig. 5: The GC sample in the pericentre versus eccentricity plane, in semilogarithmic scale. The uncertainties are computed as detailed in Sec. 3.3. The GCs are marked depending on their identified progenitor as in Fig. 2.

4.9. Other structures

As already pointed out, the wealth of data that became available roughly in the last decade has allowed to populate much more the different dynamical parameter spaces and highlight smaller confirmed merger events (and candidates). The following progenitors have only a small number of GCs associated to each of them.

4.9.1. Aleph

This structure appears to be a direct continuation of the disc at high energies with some of the most prograde GCs (red triangles in Fig. 2). The GCs belonging to this progenitor also exhibit higher R_{peri} and R_{apo} than their counterparts in the disc (Fig. 3). Aleph GCs have:

- $E_{tot} > -1.1 \times 10^5 \text{ km}^2/\text{s}^2$
- $R_{peri} > 5 \text{ kpc}$
- $R_{apo} > 10 \text{ kpc}$
- $Ecc < 0.4$
- $L_z < -1.75 \times 10^3 \text{ kpc km/s}$

4.9.2. Cetus

This merger, identified as a stream on a very polar orbit, is composed of prograde and very energetic tracers, very close to Sag in $L_z - E_{tot}$ space (purple triangles in Fig. 2). It is possible to distinguish the genuine members of the Cetus merger for their extremely high R_{peri} , R_{apo} (Fig. 3), L_{\perp} (Fig. 6) and almost fully polar orbits (Fig. 4). The GCs belonging to Cetus have:

- $E_{tot} > -0.5 \times 10^5 \text{ km}^2/\text{s}^2$
- $L_z \approx -2.0 \times 10^3 \text{ kpc km/s}$
- $L_{\perp} > 11.0 \times 10^3 \text{ kpc km/s}$

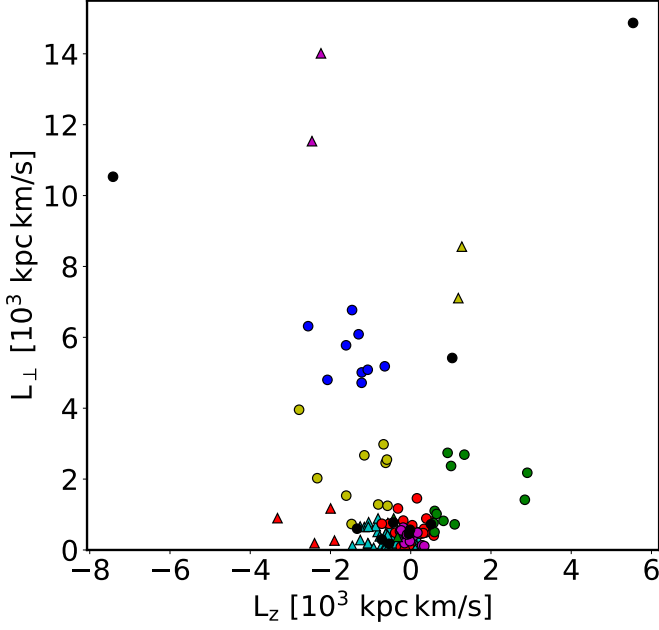


Fig. 6: The GC sample in the vertical versus perpendicular angular momentum plane. As clear by this figure, the majority of GCs are crowded in the low L_{\perp} region, with the loci of different progenitors overlapping, but this space is very helpful to distinguish the various high energy families. The GCs are marked depending on their identified progenitor as in Fig. 2.

4.9.3. Typhon

This is another merger discovered as a surviving stream with a long, radial orbit. We tentatively associate two high energy GCs to this progenitor. These GCs partially overlap in some parameter spaces with the Typhon stellar populations identified by Tenachi et al. (2022) and Dodd et al. (2023) and are characterised by radial orbits (green triangles in Fig. 4) and very high R_{apo} coupled to very low R_{peri} (Fig. 3). We tentatively identify as Typhon GCs those having:

- $E_{tot} > -0.7 \times 10^5 \text{ km}^2/\text{s}^2$
- $1.0 \text{ kpc} < R_{peri} < 2.0 \text{ kpc}$
- $R_{apo} > 50 \text{ kpc}$
- $Z_{max} > 40 \text{ kpc}$

4.9.4. Elqui

The stream of debris produced by this merger is one of the most distant identified (Shipp et al. 2018, 2019). The associated GCs are retrograde and at high energies (yellow triangles in Fig. 2) but they have much higher R_{peri} , R_{apo} (Fig. 3), and L_{\perp} (Fig. 6) with respect to the retrograde group. Being quite isolated from the rest of the retrograde family in almost all dynamical spaces, we are confident in assigning two GCs directly to Elqui. These GCs have:

- $E_{tot} > -0.5 \times 10^5 \text{ km}^2/\text{s}^2$
- $L_z \approx 1.0 \times 10^3 \text{ kpc km/s}$
- $7.0 \times 10^3 \text{ kpc km/s} < L_{\perp} < 9.0 \times 10^3 \text{ kpc km/s}$

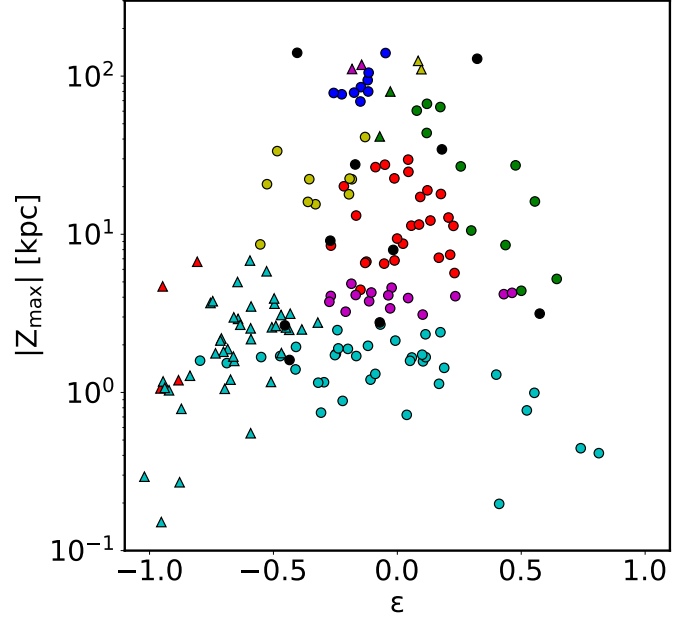


Fig. 7: The GC sample in the circularity versus maximum vertical excursion plane, in semilogarithmic scale. The GCs are marked depending on their identified progenitor as in Fig. 2.

5. Discussion

The main difference between this work and most in the literature is the presence of the rotating bar of the MW in the model underlying the orbital integration. We tested the direct effect of including/excluding the bar by running ORBIT with and without the rotating bar and noting the differences in the outputs. The main effect of the bar is in changing pericentres and eccentricities for GCs roughly below $E_{tot} = -1.7 \times 10^5 \text{ km}^2/\text{s}^2$ and for some of those with highly radial orbits (i.e. very small pericentres). This translates into some changes in the classification of the GCs in the lowest energy groups (bulge, disc, GES and low-energy) but leaves basically untouched the classification of the GCs belonging to the other families. Without the bar Gran 5, NGC 6517, NGC 6626 (all previously classified bulge GCs), NGC 6121 (previously GES), NGC 6723 (previously unclassified), and NGC 6171 (previously disc) would be classified as low-energy GCs. Three clusters (NGC 6256, NGC 6266 and NGC 6540) would move from the bulge to the disc family and one (2MASS-GC02) would move from the disc to the bulge family. Finally, NGC 6284 would be identified as a GES member. These changes in associations of GCs and progenitors make our whole classification much closer to literature ones (i.e. Massari et al. 2019) because our model without a bar is essentially a variant of the widely used McMillan (2017) model.

5.1. Outliers within the groups

While we identified defining characteristics for each family, some members do stand out thanks to peculiar properties. In the following, we cover these and the GCs contended between groups.

Starting from the bulge, it is important to mention the small number of GCs with ϵ and J_{\parallel} values suggesting highly counter-rotating orbits (the cyan circles at the bottom right of Fig. 7 with

$\varepsilon > 0.4$). VVV-CL001, Djor 2, Terzan 2, Terzan 6, Liller 1, and NGC 6325 appear to be clearly separated from the main bulge population by their peculiar kinematics. Tests show that the spherical component of the bulge is partly responsible for their extreme kinematics, but even removing that component these GCs remain on clearly counter-rotating orbits (just not as extreme). Gran 1 stands out for another reason, as one of the least eccentric GCs of the entire sample, with a very polar orbit confined to the inner bulge (the topmost cyan circle at $J_{\perp} \approx 1.0$ in Fig. 4).

At the “interface” between the bulge and the disc groupings there are four GCs with quite circular orbits (cyan circles with $J_{\parallel} \geq 0.6$ in Fig. 4). Despite this, NGC 6256, NGC 6266, NGC 6540, and Terzan 1 reside deep into the potential well, with very small R_{apo} and R_{peri} , so we assigned them to the bulge. Conversely, 2MASS-GC02 is the least energetic of the disc GCs but its R_{apo} and R_{peri} are not low enough to make it a resident of the bulge region, so we assigned it to the disc family. Four out of five of these GCs are exactly the ones moving between the bulge and disc families depending on the presence/absence of the rotating bar (Sec. 5) and show the influence of different choices of bulge models.

Moving on to the low-E group, it is worth reminding that it has been the home of tracers that couldn’t be unambiguously attributed to either the GES or the MW bulge. Several authors linked some or all members of this group to different accretion events, Kraken (Kruijssen et al. 2019, 2020), Koala (Forbes 2020), Heracles (Horta et al. 2021), which might possibly be the same structure. Other works highlighted in-situ populations with similar chemo-kinematical signatures, Aurora (Belokurov & Kravtsov 2022; Myeong et al. 2022), Poor Old Heart (Rix et al. 2022), arguing that all these structures (accreted and in-situ) are the different facets of the same stellar population constituting the proto-Galaxy. Nevertheless, due to their quite tight distribution in dynamical parameter spaces, we have kept these clusters grouped together. The only two significant outliers in this family are NGC 6388 and NGC 6535 being the most retrograde and planar low-E GCs (they are the rightmost purple circles in Fig. 7). Both GCs, while very retrograde, don’t have enough energy to connect with the retrograde family or with the hypothesised Thamnos members (discussed in Sec. 5.2). Interestingly, they remain quite close in all parameter spaces, which might hint at a shared history.

The GES group of GCs has several slight outliers. Pal 2 is one of the most energetic GES GCs with a very radial orbit, a very low R_{peri} and very high R_{apo} (rightmost red circle in Fig. 3) and $|Z_{max}|$ but all the other parameters identify it as belonging to the GES progenitor. NGC 5904 and NGC 7492 are compatible with GES in most parameter spaces but have the highest L_{\perp} and R_{peri} of the family. Similarly, the high ecc and radial orbit of NGC 6584 identify it as a GES GC even if it has very high $|Z_{max}|$ and R_{peri} (these three GCs are the highest red circles in Fig. 3). NGC 6205 and NGC 7099 fit quite well amid the GES family except for their uncharacteristically low ecc (red circles at $ecc \approx 0.7$ in Fig. 5). Given the nature of GES as the most massive merger event of the MW, it is quite possible for its dynamical signature to not be as compact as other smaller and more recent merger events (i.e. Sag) and present a low number of outliers (6 out of 26 GCs).

Moving towards prograde and higher energy space, ESO 93-08 and Pal 10 are the two uncertain attributions to the Aleph structure (lowest red triangles in Fig. 7). While having higher E_{tot} and $|L_z|$ than disc GCs, they have much lower $|Z_{max}|$ and L_{\perp} than the other members of Aleph and therefore might be the

very outermost disc GCs. Given the uncertainty in the nature and characteristics of the Aleph progenitor, it is unclear if these GCs have a tighter link to the disc or not.

NGC 4590, NGC 5824 and NGC 6426 are the GCs on the most prograde circular orbits for the HS family (yellow circles with $J_{\parallel} < -0.5$ in Fig. 4), similar to disc GCs, but they have R_{apo} , Z_{max} , and L_{\perp} in line with the HS group and they are on the HS sequence in $R_{peri} - ecc$ space. Leaving debris with quite prograde orbits is to be expected from a merger generally believed to be prograde (even if not planar) and quite massive at the time of accretion (Helmi et al. 1999).

The Sag group is well isolated in all parameter spaces with only Eridanus being slightly an outlier for its higher $|Z_{max}|$.

5.2. The retrograde family

The retrograde halo has been populated by several candidate progenitors over the years, starting with Sequoia (Myeong et al. 2018; Barbá et al. 2019; Matsuno et al. 2019; Myeong et al. 2019) and Elqui (Shipp et al. 2018, 2019) to several more. Studies on simulations recreating the complex dynamics of galactic mergers suggest that high mass-ratio events spread their debris across large portions of parameter space, spilling copiously also in the retrograde portion of the halo, leading to these debris being mistaken for independent mergers (Koppelman et al. 2020; Amarante et al. 2022; Khoperskov et al. 2023). Arjuna (proposed by Naidu et al. 2020) has been rejected for this very reason and its sibling I’itoi (from the same work) is facing similar scrutiny, hampered by a dearth of chemical information (Naidu et al. 2021; Horta et al. 2023).

Thamnos (Koppelman et al. 2019a) is another candidate member of the retrograde family, first identified as a couple of overdensities very close to each other in the mid-energy, retrograde portion of $L_z - E_{tot}$ space. Koppelman et al. (2019a) and subsequent works estimated a very low mass for the Thamnos progenitor ($M_{Thamnos} \leq 5 \cdot 10^7 M_{\odot}$), making it very unlikely it would harbour any GC capable of surviving the merging event while keeping a recognisable dynamical signature up to the present time. Moreover, some recent works on the chemical characterisation of substructures seem to indicate that the Thamnos stellar population is heavily contaminated by in-situ and GES tracers (i.e. Fig. 15 from Ruiz-Lara et al. 2022). Nevertheless, based on a purely dynamical analysis, there are several clusters unassociated with other progenitors or within the retrograde family that fall into or near the loci identified by the Thamnos stellar component in the various dynamical spaces. NGC 5139 (also known as ω Cen) and FSR 1758 are the GCs that track more closely the Thamnos stellar population across all parameter spaces while Gran 2 exhibits a slightly out-of-plane, more polar orbit (with higher $|Z_{max}|$ and L_{\perp}). The aforementioned NGC 6388 and NGC 6535 have retrograde, planar orbits very similar to the Thamnos tracers but they reside much deeper in the MW potential well and have lower E_{tot} , R_{apo} and R_{peri} .

Antaeus/L-RL64 is an extremely retrograde and highly energetic merger remnant identified by Oria et al. (2022) and Ruiz-Lara et al. (2022). More recently, the small structure of ED-3 has been identified in the retrograde halo (Dodd et al. 2023), occupying loci connected or contiguous to Antaeus/L-RL64 in all parameter spaces. The association of the two structures has been corroborated by the findings of Ceccarelli et al. (2024). Based on their heavily retrograde orbits, NGC 3201 and NGC 6101 could be associated with this structure. Even if the two clusters don’t directly track the stars identified as Antaeus members by Oria et al. (2022) and Dodd et al. (2022), NGC

3201 follows quite closely the loci of the ED-3 members in all dynamical spaces, allowing us to establish a tentative association between the two GCs and the Antaeus progenitor.

5.3. Unclassified GCs

Some MW GCs share some defining characteristics with the above mentioned groups but also appear to be very discordant in other parameter spaces. We will quickly review this list of outliers that cannot be unequivocally assigned to one of the progenitors.

AM-4 sits amid the retrograde group in $L_z - E_{tot}$ but has much higher R_{peri} and much lower ecc that distinguish it as a clear extreme outsider to this family. Crater is too extreme in all parameter spaces to be a part of any retrograde family. Sag II is Crater’s counterpart in the prograde portion of dynamical space, being a distant outlier from all identified groups. NGC 6934 is too energetic for, and has an higher R_{apo} than, Helmi Streams GCs but has R_{peri} and $|Z_{max}|$ too low for Sag GCs and its orbit is too radial for both families. Sitting between the loci of the low-energy and GES families, NGC 6284 has R_{apo} , R_{peri} , and $|Z_{max}|$ too high to belong to the former group and ecc too low, coupled to an orbit more polar than radial, to be a GES GC. BH 140 and Djor 1 have many characteristics of disc GCs, with prograde, circular orbits, but their R_{apo} , R_{peri} , and ecc are too high compared to the other disc GCs. The orbit of NGC 5897 is not circular enough for it to be a (thick) disc GC and not radial enough to belong to the GES. Similarly, its R_{apo} , R_{peri} , and $|Z_{max}|$ are too high for the disc and its ecc is too low for the GES. Gran 3 has a retrograde, circular, very low ecc orbit that sets it apart, at its energy range, from nearby identified groups. NGC 6723 similarly has a very low ecc (so it is very improbable that it belongs to the low-E group) and is characterised by a peculiar, extremely polar orbit.

5.4. Literature comparison

Reviewing some recent literature on the classification of the MW GC population, we don’t do a direct comparison with the work of Bica et al. (2024) as they used a selection base on ages and chemistry, while we used purely dynamical information. Similarly, the selection done by Belokurov & Kravtsov (2024), while taking into account the dynamical component, is guided and calibrated using the $[Al/Fe]$ abundance ratio and only distinguishes between the in-situ and accreted component. Nevertheless we generally agree on the classification by Belokurov & Kravtsov (2024), with the notable exception of the low-E family (whose members the authors mostly classify as in-situ, probably attributing them to the Aurora population, Belokurov & Kravtsov 2022). For the families identified in both works, we also find general agreement with the classification by Chen & Gnedin (2024), again with the notable exception of the low-E group, identified as in-situ by these authors. Our results closely agree with the classification of the high- and mid-energy GCs of Callingham et al. (2022); Sun et al. (2023); Massari (2025), but we have different findings in the lowest energy groups (bulge, disc, low-E). All these works use an underlying McMillan (2017) static potential and is clear that the discrepancies in the classification of the least energetic GCs depend on the impact of the rotating bar on the orbital parameters. In the case of Massari (2025) it is worth also noting that part of the differences are due to the authors not including Aleph in their list of progenitors and in us slightly unpacking their “high energy” group into some known progenitors (and Typhon). We note several differ-

ences with respect to the classification made by Malhan et al. (2022) and the principal reason is the use of a partially different set of progenitors, namely LMS-1/Wukong, Pontus and an unknown retrograde merger (see Sec. 4.1 for our reasons to not include these progenitors in our list). One of the first works on the topic to use an underlying potential including a rotating bar is Pérez-Villegas et al. (2020) but they use a different classification (bulge, disc, inner halo, outer halo) and don’t discriminate between the various merger events. Nevertheless our results closely agree in the list of bulge and disc clusters, with minor discrepancies due to the different cut in ecc used to determine if a GC belongs to the disc or not. Another work including a rotating bar in the underlying potential is Garro et al. (2023), working on a small subsample of clusters. Our results are in general agreement with theirs, with orbital parameters consistent within the errors.

6. Conclusions

We have presented ORBIT, a new in-house tool aimed at precise and efficient orbit integration for the study of the galactic dynamics. The novelty of the code resides in fully accounting for a time-varying potential at all stages, especially for the recovery of the orbital parameters and their associated errors. ORBIT, with its up-to-date potential model of the MW including the rotating bar and a spherical bulge component, has already been used to characterise the RR Lyrae population of the bulge (Olivares Carvajal et al. 2024). Here, we used ORBIT to study the dynamics of the galactic GCs and to classify them among the various families of merger events.

By using the information derived from six different dynamical parameter spaces (of orbital parameters, IoMs and adiabatic invariants), we provided a full dynamical characterisation of the in-situ population and of the different progenitors. The inclusion of the rotating bar changes the associations of low energy GCs while the full dynamical picture painted by our results allows for clear associations for a number of previously unassociated high energy GCs to various structures (4 GCs to Aleph and 2 each to Cetus, Typhon, Elqui and Antaeus).

We also proposed the association of 3 GCs to the Thamnos progenitor, further complicating the conundrum represented by this very small old merger.

A number of GCs remain of ambiguous ancestry or are clear outliers inside their families and some are still without any associated progenitor. This work is but a stepping stone in the process of thorough characterisation of the MW inventory and our purely dynamical view has to be complemented with cutting edge chronochemical studies (i.e. the CARMA project, Massari et al. 2023; Aguado-Agelet et al. 2025; Ceccarelli et al. 2025).

In future work we will explore in more depth the effect of the rotating bar, both with its direct gravitational pull affecting the central region of the MW and with the resonances it generates as a time-varying component of the potential.

Acknowledgements. The authors would like to thank the anonymous referee for insightful comments that helped improve and clarify the manuscript. Thanks also go to D. Massari, E. Ceccarelli, M. Bellazzini, A. Mucciarelli and E. Dodd for valuable discussions. MDL acknowledges financial support from the National Agency for Research and Development (ANID), Millennium Science Initiative, ICN12_009 and from the project “LEGO – Reconstructing the building blocks of the Galaxy by chemical tagging” (PI: Mucciarelli) granted by the Italian MUR through contract PRIN2022LLP8TK_001. MZ acknowledges support by the National Agency for Research and Development (ANID) Millennium Science Initiative, ICN12_009 and AIM23-0001, awarded to the Millennium Institute of Astrophysics (MAS) and the ANID BASAL Center for Astrophysics and Associated Technologies (CATA) through grant FB210003, and from ANID FONDECYT Regular No. 1230731. BA-T acknowledges support from the ANID Doc-

toral Fellowship through grant number 21231305. FG gratefully acknowledges support from the French National Research Agency (ANR) funded projects “MWDisc” (ANR-20-CE31-0004) and “Pristine” (ANR-18-CE31-0017). This research made use of the Astropy (Astropy Collaboration et al. 2013, 2018), Matplotlib (Hunter 2007) and Numpy (Harris et al. 2020) packages.

Data Availability

The data underlying this article come from public sources listed in Section 2. Table C.1 is only available in electronic form at the CDS via anonymous ftp to cdsarc.u-strasbg.fr (130.79.128.5) or via <http://cdsweb.u-strasbg.fr/cgi-bin/qcat?J/A+A/> (an excerpt of the table is provided in Appendix C).

References

- Abadi, M. G., Navarro, J. F., Steinmetz, M., & Eke, V. R. 2003, *ApJ*, 597, 21
- Aguado-Agelet, F., Massari, D., Monelli, M., et al. 2025, *arXiv e-prints*, arXiv:2502.20436
- Amarante, J. A. S., Debattista, V. P., Beraldo e Silva, L., Laporte, C. F. P., & Deg, N. 2022, *ApJ*, 937, 12
- Astropy Collaboration, Price-Whelan, A. M., Sipőcz, B. M., et al. 2018, *AJ*, 156, 123
- Astropy Collaboration, Robitaille, T. P., Tollerud, E. J., et al. 2013, *A&A*, 558, A33
- Atkinson, K. E. 1991, *An Introduction to Numerical Analysis*, Second Edition (John Wiley & Sons)
- Bacon, R., Accardo, M., Adjali, L., et al. 2010, in *Society of Photo-Optical Instrumentation Engineers (SPIE) Conference Series*, Vol. 7735, Ground-based and Airborne Instrumentation for Astronomy III, ed. I. S. McLean, S. K. Ramsay, & H. Takami, 773508
- Barbá, R. H., Minniti, D., Geisler, D., et al. 2019, *ApJ*, 870, L24
- Baumgardt, H. 2017, *MNRAS*, 464, 2174
- Baumgardt, H. & Hilker, M. 2018, *MNRAS*, 478, 1520
- Baumgardt, H. & Vasiliev, E. 2021, *MNRAS*, 505, 5957
- Belokurov, V., Erkal, D., Evans, N. W., Koposov, S. E., & Deason, A. J. 2018, *MNRAS*, 478, 611
- Belokurov, V. & Kravtsov, A. 2022, *MNRAS*, 514, 689
- Belokurov, V. & Kravtsov, A. 2024, *MNRAS*, 528, 3198
- Bennett, M. & Bovy, J. 2019, *MNRAS*, 482, 1417
- Bensby, T., Feltzing, S., & Oey, M. S. 2014, *A&A*, 562, A71
- Bica, E., Ortolani, S., Barbay, B., & Oliveira, R. A. P. 2024, *A&A*, 687, A201
- Binney, J. & Tremaine, S. 2008, *Galactic Dynamics: Second Edition* (Princeton University Press)
- Bovy, J. 2015, *ApJS*, 216, 29
- Bullock, J. S. & Johnston, K. V. 2005, *ApJ*, 635, 931
- Callingham, T. M., Cautun, M., Deason, A. J., et al. 2022, *MNRAS*, 513, 4107
- Ceccarelli, E., Massari, D., Aguado-Agelet, F., et al. 2025, *arXiv e-prints*, arXiv:2503.02939
- Ceccarelli, E., Massari, D., Mucciarelli, A., et al. 2024, *A&A*, 684, A37
- Chandrasekhar, S. 1943a, *ApJ*, 97, 255
- Chandrasekhar, S. 1943b, *ApJ*, 97, 263
- Chandrasekhar, S. 1943c, *ApJ*, 98, 54
- Chen, Y. & Gnedin, O. Y. 2024, *The Open Journal of Astrophysics*, 7, 23
- Chiba, R., Friske, J. K. S., & Schönrich, R. 2021, *MNRAS*, 500, 4710
- Chiba, R. & Schönrich, R. 2021, *MNRAS*, 505, 2412
- Dillamore, A. M., Belokurov, V., & Evans, N. W. 2024, *MNRAS*, 532, 4389
- Dillamore, A. M. & Sanders, J. L. 2025, *MNRAS*, 542, 1331
- Dodd, E., Callingham, T. M., Helmi, A., et al. 2022, *VizieR Online Data Catalog: Gaia DR3 of substructure in the stellar halo (Dodd+, 2023)*, *VizieR On-line Data Catalog: J/A+A/670/L2*. Originally published in: 2023A&A...670L...2D
- Dodd, E., Callingham, T. M., Helmi, A., et al. 2023, *A&A*, 670, L2
- EGgen, O. J., Lynden-Bell, D., & Sandage, A. R. 1962, *ApJ*, 136, 748
- Forbes, D. A. 2020, *MNRAS*, 493, 847
- Forbes, D. A. & Bridges, T. 2010, *MNRAS*, 404, 1203
- Gaia Collaboration, Prusti, T., de Bruijne, J. H. J., et al. 2016, *A&A*, 595, A1
- Gaia Collaboration, Vallenari, A., Brown, A. G. A., et al. 2023, *A&A*, 674, A1
- Garro, E. R., Fernández-Trincado, J. G., Minniti, D., et al. 2023, *A&A*, 669, A136
- Garro, E. R., Minniti, D., Alessi, B., et al. 2022, *A&A*, 659, A155
- Gómez, F. A., Helmi, A., Brown, A. G. A., & Li, Y.-S. 2010, *MNRAS*, 408, 935
- Gran, F., Kordopatis, G., Zoccali, M., et al. 2024, *A&A*, 683, A167
- Gran, F., Zoccali, M., Saviane, I., et al. 2022, *MNRAS*, 509, 4962
- GRAVITY Collaboration, Abuter, R., Amorim, A., et al. 2019, *A&A*, 625, L10
- Hairer, E., Lubich, C., & Wanner, G. 2003, *Acta Numerica*, 12, 399
- Harris, C. R., Millman, K. J., van der Walt, S. J., et al. 2020, *Nature*, 585, 357
- Hartke, J., Kakkad, D., Reyes, C., et al. 2020, in *Society of Photo-Optical Instrumentation Engineers (SPIE) Conference Series*, Vol. 11448, Adaptive Optics Systems VII, ed. L. Schreiber, D. Schmidt, & E. Vernet, 114480V
- Hayden, M. R., Bovy, J., Holtzman, J. A., et al. 2015, *ApJ*, 808, 132
- Haywood, M., Di Matteo, P., Lehnert, M. D., et al. 2018, *ApJ*, 863, 113
- Haywood, M., Khoperskov, S., Cerqui, V., et al. 2024, *A&A*, 690, A147
- Helmi, A., Babusiaux, C., Koppelman, H. H., et al. 2018, *Nature*, 563, 85
- Helmi, A. & de Zeeuw, P. T. 2000, *MNRAS*, 319, 657
- Helmi, A. & White, S. D. M. 1999, *MNRAS*, 307, 495
- Helmi, A., White, S. D. M., de Zeeuw, P. T., & Zhao, H. 1999, *Nature*, 402, 53
- Horta, D., Schiavon, R. P., Mackereth, J. T., et al. 2021, *MNRAS*, 500, 1385
- Horta, D., Schiavon, R. P., Mackereth, J. T., et al. 2023, *MNRAS*, 520, 5671
- Hunter, J. D. 2007, *Computing in Science and Engineering*, 9, 90
- Ibata, R. A., Gilmore, G., & Irwin, M. J. 1994, *Nature*, 370, 194
- Khoperskov, S., Minchev, I., Libeskind, N., et al. 2023, *A&A*, 677, A90
- Koppelman, H., Helmi, A., & Veljanoski, J. 2018, *ApJ*, 860, L11
- Koppelman, H. H., Bos, R. O. Y., & Helmi, A. 2020, *A&A*, 642, L18
- Koppelman, H. H., Helmi, A., Massari, D., Price-Whelan, A. M., & Starkenburg, T. K. 2019a, *A&A*, 631, L9
- Koppelman, H. H., Helmi, A., Massari, D., Roelenga, S., & Bastian, U. 2019b, *A&A*, 625, A5
- Kruijssen, J. M. D., Pfeffer, J. L., Chevance, M., et al. 2020, *MNRAS*, 498, 2472
- Kruijssen, J. M. D., Pfeffer, J. L., Reina-Campos, M., Crain, R. A., & Bastian, N. 2019, *MNRAS*, 486, 3180
- Leaman, R., VandenBerg, D. A., & Mendel, J. T. 2013, *MNRAS*, 436, 122
- Lian, J., Zasowski, G., Mackereth, T., et al. 2022, *MNRAS*, 513, 4130
- Lim, D., Koch-Hansen, A. J., Chung, C., et al. 2021, *A&A*, 647, A34
- Long, K. & Murali, C. 1992, *ApJ*, 397, 44
- Lövdal, S. S., Ruiz-Lara, T., Koppelman, H. H., et al. 2022, *A&A*, 665, A57
- Mace, G., Sokal, K., Lee, J.-J., et al. 2018, in *Society of Photo-Optical Instrumentation Engineers (SPIE) Conference Series*, Vol. 10702, Ground-based and Airborne Instrumentation for Astronomy VII, ed. C. J. Evans, L. Simard, & H. Takami, 107020Q
- Majewski, S. R., Schiavon, R. P., Frinchaboy, P. M., et al. 2017, *AJ*, 154, 94
- Majewski, S. R., Skrutskie, M. F., Weinberg, M. D., & Ostheimer, J. C. 2003, *ApJ*, 599, 1082
- Malhan, K. 2022, *ApJ*, 930, L9
- Malhan, K., Ibata, R. A., Sharma, S., et al. 2022, *ApJ*, 926, 107
- Malhan, K. & Rix, H.-W. 2024, *ApJ*, 964, 104
- Malhan, K., Yuan, Z., Ibata, R. A., et al. 2024, *VizieR Online Data Catalog: Stars of the LMS-1 stream with sp. obs. (Malhan+, 2021)*, *VizieR On-line Data Catalog: J/ApJ/920/51*. Originally published in: 2021ApJ...920...51M
- Marín-Franch, A., Aparicio, A., Piotto, G., et al. 2009, *ApJ*, 694, 1498
- Massari, D. 2025, *Research Notes of the American Astronomical Society*, 9, 64
- Massari, D., Aguado-Agelet, F., Monelli, M., et al. 2023, *A&A*, 680, A20
- Massari, D., Koppelman, H. H., & Helmi, A. 2019, *A&A*, 630, L4
- Matsuno, T., Aoki, W., & Suda, T. 2019, *ApJ*, 874, L35
- McKee, C. F., Parravano, A., & Hollenbach, D. J. 2015, *ApJ*, 814, 13
- McMillan, P. J. 2017, *MNRAS*, 465, 76
- Minniti, D., Fernández-Trincado, J. G., Smith, L. C., et al. 2021, *A&A*, 648, A86
- Minniti, D., Lucas, P. W., Emerson, J. P., et al. 2010, *New A*, 15, 433
- Minniti, D., Matsunaga, N., Fernández-Trincado, J. G., et al. 2024, *A&A*, 683, A150
- Miyamoto, M. & Nagai, R. 1975, *PASJ*, 27, 533
- Moni Bidin, C., Mauro, F., Geisler, D., et al. 2011, *A&A*, 535, A33
- Moreno, E., Fernández-Trincado, J. G., Pérez-Villegas, A., Chaves-Velasquez, L., & Schuster, W. J. 2022, *MNRAS*, 510, 5945
- Myeong, G. C., Belokurov, V., Aguado, D. S., et al. 2022, *ApJ*, 938, 21
- Myeong, G. C., Evans, N. W., Belokurov, V., Sanders, J. L., & Koposov, S. E. 2018, *MNRAS*, 478, 5449
- Myeong, G. C., Vasiliev, E., Iorio, G., Evans, N. W., & Belokurov, V. 2019, *MNRAS*, 488, 1235
- Naidu, R. P., Conroy, C., Bonaca, A., et al. 2020, *ApJ*, 901, 48
- Naidu, R. P., Conroy, C., Bonaca, A., et al. 2021, *ApJ*, 923, 92
- Navarro, J. F., Frenk, C. S., & White, S. D. M. 1996, *ApJ*, 462, 563
- Necib, L., Ostdiek, B., Lisanti, M., et al. 2020a, *ApJ*, 903, 25
- Necib, L., Ostdiek, B., Lisanti, M., et al. 2020b, *Nature Astronomy*, 4, 1078
- Necib, L., Ostdiek, B., Lisanti, M., et al. 2022, *Nature Astronomy*, 6, 866
- Newberg, H. J., Yanny, B., & Willett, B. A. 2009, *ApJ*, 700, L61
- Olivares Carvajal, J., Zoccali, M., De Leo, M., et al. 2024, *A&A*, 687, A312
- Olivares Carvajal, J., Zoccali, M., Rojas-Arriagada, A., et al. 2022, *MNRAS*, 513, 3993
- Oria, P.-A., Tenachi, W., Ibata, R., et al. 2022, *ApJ*, 936, L3
- Orkney, M. D. A., Laporte, C. F. P., Grand, R. J. J., et al. 2023, *MNRAS*, 525, 683
- Pagnini, G., Di Matteo, P., Khoperskov, S., et al. 2023, *A&A*, 673, A86

- Park, C., Jaffe, D. T., Yuk, I.-S., et al. 2014, in Society of Photo-Optical Instrumentation Engineers (SPIE) Conference Series, Vol. 9147, Ground-based and Airborne Instrumentation for Astronomy V, ed. S. K. Ramsay, I. S. McLean, & H. Takami, 91471D
- Peebles, P. J. E. 1965, *ApJ*, 142, 1317
- Peebles, P. J. E. & Yu, J. T. 1970, *ApJ*, 162, 815
- Pérez-Villegas, A., Barbuy, B., Kerber, L. O., et al. 2020, *MNRAS*, 491, 3251
- Plummer, H. C. 1911, *MNRAS*, 71, 460
- Prudil, Z., Kunder, A., Beraldo e Silva, L., et al. 2025, *A&A*, 695, A211
- Queiroz, A. B. A., Chiappini, C., Perez-Villegas, A., et al. 2021, *A&A*, 656, A156
- Re Fiorentin, P., Spagna, A., Lattanzi, M. G., & Cignoni, M. 2021, *ApJ*, 907, L16
- Re Fiorentin, P., Spagna, A., Lattanzi, M. G., Cignoni, M., & Vitali, S. 2024, *ApJ*, 977, 278
- Read, J. I., Pontzen, A. P., & Viel, M. 2006, *MNRAS*, 371, 885
- Reid, M. J. 2008, in IAU Symposium, Vol. 248, A Giant Step: from Milli- to Micro-arcsecond Astrometry, ed. W. J. Jin, I. Platais, & M. A. C. Perryman, 141–147
- Rix, H.-W., Chandra, V., Andrae, R., et al. 2022, *ApJ*, 941, 45
- Roberts, J. A. G. & Quispel, G. R. W. 1992, *Phys. Rep.*, 216, 63
- Ruchti, G. R., Read, J. I., Feltzing, S., Pipino, A., & Bensby, T. 2014, *MNRAS*, 444, 515
- Ruiz-Lara, T., Matsuno, T., Lövdal, S. S., et al. 2022, *A&A*, 665, A58
- Saito, R. K., Hempel, M., Minniti, D., et al. 2012, *A&A*, 537, A107
- Sanders, J. L., Smith, L., & Evans, N. W. 2019, *MNRAS*, 488, 4552
- Schönrich, R., Binney, J., & Dehnen, W. 2010, *MNRAS*, 403, 1829
- Searle, L. & Zinn, R. 1978, *ApJ*, 225, 357
- Shen, J. & Zheng, X.-W. 2020, *Research in Astronomy and Astrophysics*, 20, 159
- Shipp, N., Drlica-Wagner, A., Balbinot, E., et al. 2018, *ApJ*, 862, 114
- Shipp, N., Li, T. S., Pace, A. B., et al. 2019, *ApJ*, 885, 3
- Ströbele, S., La Penna, P., Arsenault, R., et al. 2012, in Society of Photo-Optical Instrumentation Engineers (SPIE) Conference Series, Vol. 8447, Adaptive Optics Systems III, ed. B. L. Ellerbroek, E. Marchetti, & J.-P. Véran, 844737
- Stuik, R., Bacon, R., Conzelmann, R., et al. 2006, *New A Rev.*, 49, 618
- Sun, G., Wang, Y., Liu, C., et al. 2023, *Research in Astronomy and Astrophysics*, 23, 015013
- Tenachi, W., Oria, P.-A., Ibata, R., et al. 2022, *ApJ*, 935, L22
- Trick, W. H. 2022, *MNRAS*, 509, 844
- Valenti, E., Zoccali, M., Gonzalez, O. A., et al. 2016, *A&A*, 587, L6
- Vasiliev, E. 2019a, *MNRAS*, 482, 1525
- Vasiliev, E. 2019b, *MNRAS*, 484, 2832
- Vasiliev, E. & Baumgardt, H. 2021, *MNRAS*, 505, 5978
- Verlet, L. 1967, *Physical Review*, 159, 98
- Wang, S., Necib, L., Ji, A. P., et al. 2023, *ApJ*, 955, 129
- Wegg, C., Gerhard, O., & Portail, M. 2015, *MNRAS*, 450, 4050
- White, S. D. M. & Rees, M. J. 1978, *MNRAS*, 183, 341
- Woudenberg, H. C. & Helmi, A. 2025, *A&A*, 700, A240
- Yuan, Z., Chang, J., Beers, T. C., & Huang, Y. 2020, *ApJ*, 898, L37
- Yuan, Z., Malhan, K., Sestito, F., et al. 2022, *ApJ*, 930, 103
- Yuan, Z., Smith, M. C., Xue, X.-X., et al. 2019, *ApJ*, 881, 164
- Zinn, R. 1985, *ApJ*, 293, 424
- Zinn, R. 1996, in Astronomical Society of the Pacific Conference Series, Vol. 92, Formation of the Galactic Halo...Inside and Out, ed. H. L. Morrison & A. Sarajedini, 211
- Zoccali, M., Quezada, C., Contreras Ramos, R., et al. 2024, *A&A*, 689, A240
- Zoccali, M., Valenti, E., & Gonzalez, O. A. 2018, *A&A*, 618, A147

Appendix A: Impact of observational errors: worst cases

As mentioned in Sec. 2, we tested that our results (the attribution of each GC to a specific progenitor) are robust even when taking into account observational errors. Here we show the worst cases out of the entire sample, even for them the classification doesn't become ambiguous when taking into account the uncertainties. In Fig. A.1 we show the high energy GCs AM 1 (grey star), Eridanus (blue star), Palomar 3 (red star) and Palomar 4 (orange star), the GCs with the highest distance uncertainties, in the $L_z - L_\perp$ space. The underlying coloured contours in the same tonalities (greys for AM 1, blues for Eridanus, etc...) show the density distribution of 1000 integrations with different input phase space values generated by extracting from the error distributions of each GC. We also show the nearest progenitor families (Sag, HS, the retrogrades, and the other Elqui member). It is clear from the figure that, even for the cases with the largest scatter (AM 1, Palomar 4), accounting for the errors doesn't change the classification of these GCs. Similarly, in Fig. A.2 we show 2MASS-GC01 (red star) and Patchick 122 (green star), the GCs with the highest uncertainties on their velocity vector, in $\varepsilon - Z_{\max}$ space. The underlying matching coloured contours show the density distribution of 1000 iterations accounting for the observational errors. As before, we also show the nearest progenitor families (bulge, disc, and low-E) and it appears clear that, even accounting for the errors, the two GCs cannot be identified as anything but disc GCs.

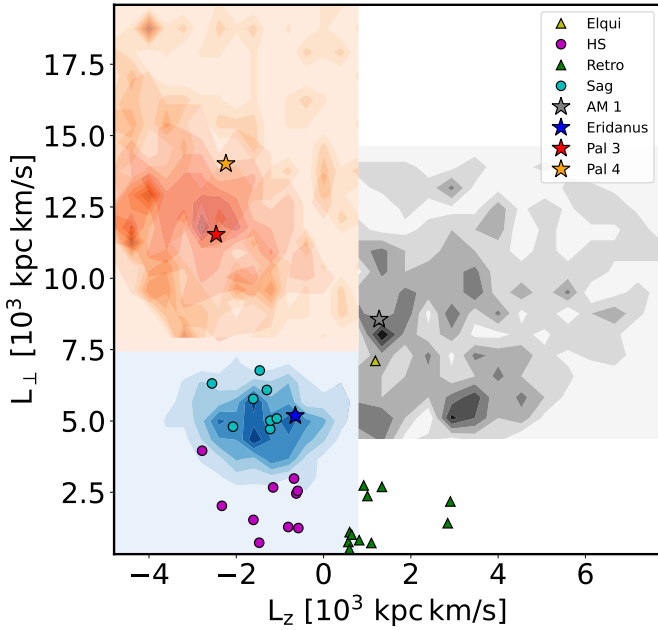


Fig. A.1: $L_z - L_\perp$ space distribution of the GCs with the highest distance uncertainties (filled stars). The underlying matching coloured contours are the distributions of 1000 iterations accounting for the observational errors. The other filled symbols (circles, triangles) are the GCs members of the nearby progenitor families.

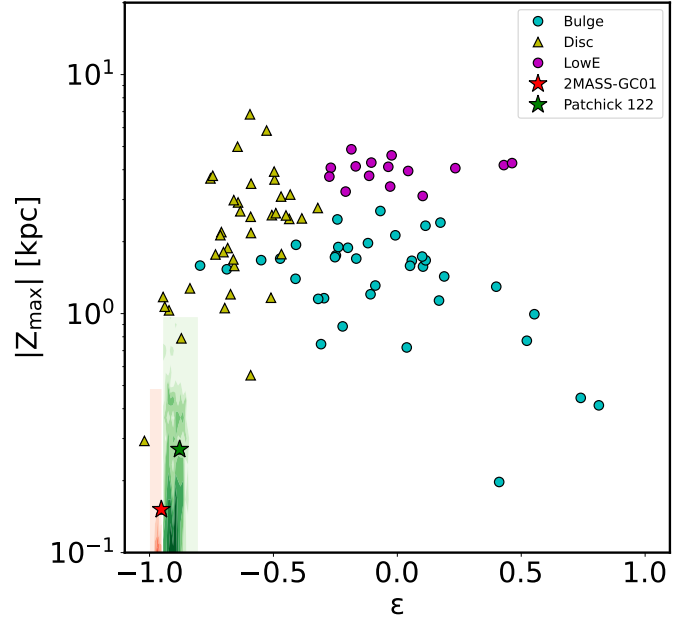


Fig. A.2: $\varepsilon - Z_{\max}$ space distribution of the GCs with the highest velocity vector uncertainties (filled stars). The underlying matching coloured contours are the distributions of 1000 iterations accounting for the observational errors. The other filled symbols (circles, triangles) are the GCs members of the nearby progenitor families.

Appendix B: Sanity checks and tests of ORBIT

To ensure that ORBIT works properly we performed an extensive array of tests, both in configurations with a symmetric and static potential (excluding the rotating bar and the central BH) and with the full time-evolving model. In the static and symmetric case, we checked the conservation of the 2 IoMs, the total mechanical energy $E_{\text{tot}} = K + U$ and the angular momentum around the symmetry axis, L_z . With the full model, the only surviving IoM is the Jacobi energy (or Jacobi integral Binney & Tremaine 2008), $E_J = E_{\text{tot}} - \Omega_b \cdot L$ (where Ω_b is the pattern speed of the rotation and L is the angular momentum corresponding to the axis of rotation, in our case L_z). Fig. B.1 shows the ratios of the variation of the three IoMs during integrations of $5 \cdot 10^6$ steps for a total of 5 Gyr. The ratios are computed as $\Delta X/X_0$ with the variation of each IoM being the value at every step minus the initial value, $\Delta X = X - X_0$ (with X being one of E_{tot} , L_z , E_J).

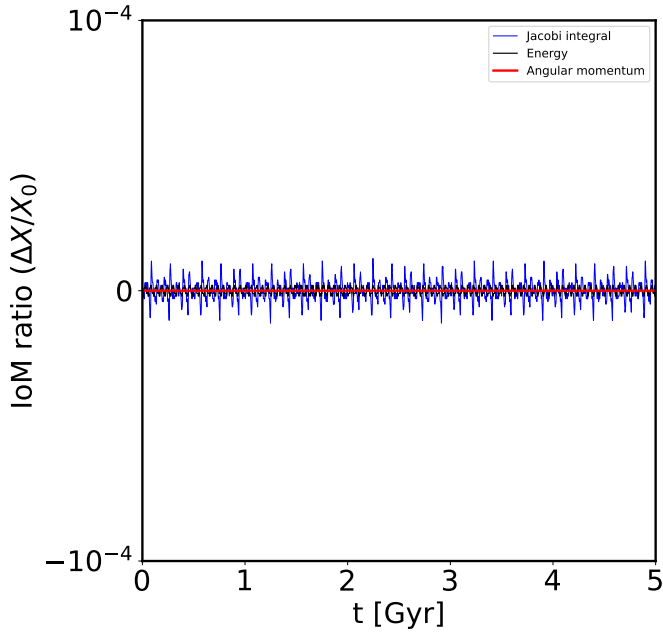


Fig. B.1: Evolution of the IoMs over a typical orbital integration. In black and red, respectively, the total mechanical energy E_{tot} and the angular momentum L_z for the case with a symmetric and static potential. In blue the Jacobi integral E_J for the case with the full potential.

Appendix C: Data table

Table C.1 is an excerpt of the results derived by ORBIT, the full table is only available in electronic form at the CDS..

Table C.1: Recovered orbital parameters, IoMs, adiabatic invariants, and derived quantities used for this analysis for each GC studied. The full table is available at the CDS.

Cluster	R_{peri} [kpc]	R_{apo} [kpc]	ecc	$ Z_{\text{max}} $ [kpc]	E_{tot} [km ² /s ²]	L_z [kpc km/s]	L_{\perp} [kpc km/s]	J_{\parallel}	J_{\perp}	ε
2MASS-GC01	2.54 ± 0.90	4.90 ± 0.21	0.34 ± 0.15	0.15	-148604.9	-924.6027	62.08	-0.96	-0.04	-0.95
2MASS-GC02	1.19 ± 0.59	2.79 ± 0.28	0.43 ± 0.25	1.17	-195646.9	-217.38	84.90	-0.68	-0.22	-0.51
AM 1	38.08 ± 13.46	167.96 ± 59.38	0.84 ± 0.30	110.59	-32665.03	1273.80	8558.58	0.10	0.27	0.10
AM 4	26.45 ± 2.04	37.72 ± 2.91	0.19 ± 0.02	34.41	-59019.18	1034.26	5417.18	0.18	0.77	0.18
Arp 2	21.50 ± 3.63	95.34 ± 16.12	0.74 ± 0.12	78.61	-42849.35	-1611.98	5775.14	-0.19	0.21	-0.17
BH 140	1.87 ± 0.32	11.68 ± 1.00	0.74 ± 0.03	2.65	-118729.4	-721.66	297.19	-0.53	-0.38	-0.45
BH 261	1.69 ± 0.34	2.64 ± 0.23	0.22 ± 0.13	1.05	-183308.9	-372.60	243.23	-0.77	0.07	-0.70
Crater	116.34 ± 67.17	220.74 ± 127.45	0.46 ± 0.27	128.76	-25927.12	5541.70	14870.94	0.31	0.48	0.32
Djor 1	1.31 ± 0.28	8.50 ± 0.73	0.74 ± 0.04	1.60	-133058.6	-544.76	173.68	-0.53	-0.42	-0.44
Djor 2	0.60 ± 0.04	0.78 ± 0.02	0.13 ± 0.04	0.44	-242466.5	129.15	94.67	0.77	0.14	0.74